JOURNAL OF COMPUTATIONAL PHYSICS 105, 92-107 (1993)

New Algorithms for Ultra-relativistic Numerical Hydrodynamics

V. SCHNEIDER, U. KATSCHER, D. H. RISCHKE, B. WALDHAUSER, J. A. MARUHN

Institut für Theoretische Physik der Universität Frankfurt, 6000 Frankfurt am Main, Germany

AND

C.-D. MUNZ

Institut für Neutronenphysik und Reaktorforschung, Kernforschungszentrum Karlsruhe, 7500 Karlsruhe, Germany

Received October 3, 1990; revised May 29, 1992

Two new transport algorithms for solving the one-dimensional relativistic hydrodynamic equations of motion are discussed. One of them, *relativistic HLLE*, is based on the HLLE upwind scheme, while the other is a relativistic adaptation of some kinds of flux corrected transport (FCT) algorithms. A comparison with other numerical methods used in relativistic hydrodynamics including fully implicit techniques is given. Emphasis is put on the dependence of the results on the relativistic gamma factor and on the adiabatic exponent entering the ideal gas equation of state. Future applications of the algorithms are particularly in the field of ultra-relativistic heavy ion collisions that require transport methods not critically dependent on the Lorentz gamma or the equation of state. © 1993 Academic Press, Inc.

1. INTRODUCTION

In ultra-relativistic heavy ion collisions energies of more than 100 GeV per nucleon are presently obtained [1, 2], corresponding to relativistic Lorentz gamma factors $\gamma \approx 10$, while for the future experiments in the tera electron volt regime are planned.

In the energy region below about 100 GeV per nucleon the experimental results could be well reproduced using a relativistic hydrodynamic model [3]. However, the numerical procedures used in these calculations yield difficulties if applied to ultra-relativistic collisions with $\gamma \geqslant 10$. Typical problems are related with inconsistencies in the laboratory frame quantities R (mass density), M (momentum density), and E (energy density), violating the relativistic conditions $E \geqslant R$ and $E \geqslant M$, and with calculated fluid velocities exceeding the speed of light. Norman and Winkler argue [4] that a fully implicit treatment of the relativistic hydrodynamic equations is required to obtain a consistent solution for large gamma factors. Furthermore, to reduce the effect of numerical diffusion, an adaptive co-moving mesh should be used. Implicit schemes and adaptive grids are, however, often not practicable in multi-dimensional calculations due to the large amount of CPU time required for an implicit treatment and due to the cell distortions in general multi-dimensional applications.

In this paper we consider explicit algorithms for the numerical solution of the relativistic hydrodynamic equations. In the last years a number of new shock-capturing schemes have been proposed for the non-relativistic equations of compressible fluid flow—the Euler equations. One well-known method is the flux corrected transport (FCT) algorithm of Boris and Book [5–8]. It was constructed to solve a scalar convection equation numerically. A system of conservation equations is interpreted as a set of scalar equations and the FCT algorithm is applied to each equation. The advantage of this procedure is that it can be easily applied to general systems. For the relativistic Euler equations we will present results based on two versions of the FCT algorithm: the original SHASTA scheme [5] and the LCPFCT scheme [8] recently proposed. A relativistic extension of the first was given by Graebner [3]; however, it was numerically reliable only for moderate γ-factors.

Another new algorithm is based on the simplest Godunov-type scheme for systems of conservation laws described by Harten *et al.* [9]. For the non-relativistic Euler equations Einfeldt [10] completed this scheme by proposing an appropriate way to calculate the numerical signal velocities. Hence we name it the HLLE method (see also [11]). Its relativistic extension is discussed in this paper. One major advantage of this algorithm is the possibility to include special relativistic effects a priori in the scheme itself. This is achieved by using the relativistic expression in the estimation of the minimum and maximal signal velocities. The approach of van Leer [12] is used to construct a second-order scheme based on this approximate Riemann solver. We restrict ourselves in this paper to one space dimension. Its generalization to two or three

0021-9991/93 $5.00
Copyright © 1993 by Academic Press, Inc.
All rights of reproduction in any form reserved.

dimensions is straightforward using the well-tested method of operator splitting. In the non-relativistic case these algorithms have been quite successful in resolving complex patterns of shocks as well as smooth flow (see, e.g., [13]).

The format of this paper is as follows: in Section 2 the relativistic hydrodynamic equations are defined. As usual in relativistic theories, the quantities entering these equations depend on the reference frame. Thus, in Section 3 we consider the question how to transform these quantities from the laboratory system into the rest frame of a fluid element. In Section 4 the two members of the family of FCT algorithms [5–7] are briefly discussed. A discussion of the relativistic HLLE method is provided in Section 5 and numerical test calculations are discussed extensively in Section 6. The Appendix gives a complete description of the relativistic HLLE algorithm as used in the test calculations.

2. THE RELATIVISTIC HYDRODYNAMIC EQUATIONS

The equations of relativistic hydrodynamics of an ideal fluid in one Cartesian space dimension x and formulated in a fixed reference frame are of the form (velocity of light $c \equiv 1$) [14]

$$R_t + (Rv)_x = 0, \tag{1}$$

$$M_t + (Mv + p)_x = 0, \tag{2}$$

$$E_t + (Ev + pv)_x = 0. \tag{3}$$

The indices t and x denote time and space derivatives, respectively. The reference frame can be any inertial frame, for example, the laboratory frame or a centre-of-velocity frame; its counterpart here will be the *local rest frame* of the fluid, which varies from one fluid element to the next. For simplicity we will refer to the fixed frame as the "laboratory" system, although, as mentioned, it need not be confined to this special case. The laboratory quantities R (mass density), M (momentum density), and E (energy density) are related to the quantities in the local rest frame e (energy density) and n (mass density) and to the fluid velocity v by the set of nonlinear transformations

$$R = \gamma n, \tag{4}$$

$$E = \gamma^2(e + p) - p, \tag{5}$$

$$M = \gamma^2(e + p)v, \tag{6}$$

$$\gamma^2 = \frac{1}{1 - v^2}. \tag{7}$$

The system of equations (1)–(7) is closed by specifying an equation of state $p = p(e, n)$. For the test calculations discussed in Section 6 two types of equations of state are used: The ideal gas equation of state

$$p = (\Gamma - 1)(e - n) \tag{8}$$

and its ultrarelativistic limit ($e \gg n$)

$$p = (\Gamma - 1)e, \tag{9}$$

with the adiabatic index $1 \leqslant \Gamma \leqslant 2$.

Relations (4)–(9) introduce a strong coupling between the hydrodynamic equations (1)–(3) and pose additional numerical problems, which are discussed in the next section. This is the reason why the relativistic equations are much more difficult to solve than their non-relativistic counterparts, although they are identical in the formal structure. For example, the physical constraints $E \geqslant R$, $E \geqslant M$, and $-1 \leqslant v \leqslant 1 (= c)$ have to be fulfilled in order for a solution of the relations (4)–(6) to exist.

Thus it seems that this strong coupling requires a simultaneous, i.e., an implicit solution of the set of Eqs. (1)–(9) on a Lagrangian or adaptive mesh. On the other hand, as mentioned in the Introduction, having the extension to two or three space dimensions in mind, implicit schemes may be very time consuming and co-moving grids are, in general, subject to strong distortions. Hence we decided to focus our considerations on explicit Eulerian algorithms and to base the relativistic schemes on methods which have been recently developed for the non-relativistic Euler equations and shown to be very efficient.

3. TRANSFORMATION FROM LABORATORY SYSTEM TO LOCAL REST FRAME

For given values of R, M, and E, Eqs. (4)–(6), together with the equation of state (8) and the definition of γ (7), make up a set of five equations with five unknown variables n, e, p, v, and γ, which have to be solved in each cell several times during a time step. The solution of this problem becomes a major part of the numerical effort and is a crucial ingredient of all the algorithms proposed here.

Equations (4), (7), and (8) can be inserted directly into Eqs. (5) and (6), yielding two coupled, non-linear equations in the unknowns e and v (or γ, respectively). These have, in general, to be solved by a two-dimensional root-finding procedure. However, for the ideal gas equation of state (8) the problem can be further simplified. Using simple algebraic transformations it is possible to eliminate one of the two unknown variables, yielding a polynomial of fourth order in the remaining variable. In our code we solve the equation

$$g(v) = [\Gamma v(E - Mv) - M(1 - v^2)]^2 - (1 - v^2)\, v^2(\Gamma - 1)^2\, R^2 = 0, \tag{10}$$

with $0 \leqslant v \leqslant 1$. This equation could either be solved by the analytic method of quartic equations or by iterative one-dimensional root-finding procedures. Using appropriate expressions for the lower limit v_l, the upper limit v_u, and the initial guess (starting value) v_0 the numerical root finding was found to be the faster method for a required accuracy of nine digits in v.

The expression for the lower boundary v_l can be derived inserting $R=0$ into Eq. (10):

$$v_l = \frac{1}{2M(\Gamma-1)}\left[\Gamma E - \sqrt{(\Gamma E)^2 - 4(\Gamma-1)M^2}\right]. \quad (11)$$

This is just the ultra-relativistic limit. Inspecting Eqs. (5), (6) one observes that $v = M/E$ as long as $p=0$, and $v < M/E$ if $p > 0$. Thus, a safe estimate for the upper boundary v_u is

$$v_u = \min\left(1, \frac{M}{E} + \delta\right), \quad (12)$$

$\delta \simeq 10^{-6}$. In the interval defined by v_l and v_u there is only one unique solution v of Eq. (10), while in the interval $0 \leqslant v \leqslant 1$ there is a second solution (at $v \leqslant v_l$) that is not a solution of the original set of coupled equations. It is generated by using the square of Eq. (6) in deriving Eq. (10).

A further advantage of using the boundaries v_l and v_u is that both approach zero as M approaches zero. An expression for the starting value in the iteration scheme that leads to fast convergence is

$$v_0 = \tfrac{1}{2}(v_l + v_u) + z, \quad (13)$$

with $z = \frac{1}{2}(1 - R/E)(v_l - v_u)$ for $v_l > \varepsilon$ and $z = 0$ otherwise; ε is a small number of the order of 10^{-9}. The additional term z has the effect that, for small R, the starting value is close to the solution of the ultra-relativistic problem.

Now the problem of finding the physically relevant solution of Eq. (10) can be solved by applying a Newton–Raphson root-finding procedure. An accuracy of nine digits can be achieved in at most five iterations.

Knowing v, e can be easily derived from the relation

$$e = E - vM. \quad (14)$$

γ, n, and p can then be calculated in a straightforward manner. Using the ultra-relativistic limit of the equation of state, Eq. (9), the problem can be solved analytically, yielding

$$e = \frac{1}{2(\Gamma-1)}\left[(\Gamma-2)E + \sqrt{\Gamma^2E^2 - 4(\Gamma-1)M^2}\right] \quad (15)$$

and

$$\gamma^2 = \frac{E + (\Gamma-1)e}{\Gamma e}. \quad (16)$$

4. FLUX CORRECTED TRANSPORT ALGORITHMS

In this section two hydrodynamic codes including versions of the flux corrected transport (FCT) algorithm developed by Boris and Book [5–7] are discussed. The basic idea of the FCT method is to increase the stability of an arbitrary differencing scheme by introducing a corrective nonlinear diffusion step. This numerical dissipation is of conservative form. In a succeeding antidiffusion step this diffusion is removed partially (flux limiter) to avoid spurious oscillations while retaining sharp profiles in cases of discontinuities or steep gradients. This numerical diffusion either can be introduced externally by means of an artificial viscosity term or can be inherent to the applied differencing scheme.

The SHASTA algorithm [5] is an example for an algorithm that uses a stable but diffusive difference scheme. A higher accuracy is achieved by including the phoenical variant of the FCT method [6]. It has been used with great success in the field of nuclear hydrodynamics [15]. Because the SHASTA algorithm and the FCT methods have been extensively discussed in the literaure (see [16] for a review and the references cited above) we restrict ourselves to a brief overview of the principles of the SHASTA algorithm.

Each of the hydrodynamic equations of motion is treated separately in this approach by formulating it as an advection equation,

$$U_t + (Uv)_x = f, \quad (17)$$

where U is a (generalized) density, v is the flow velocity, and f is a source term. The indices t and x denote time and space derivatives, respectively. The differencing scheme chosen in the SHASTA algorithm yields the expression for the transported density $\bar{U}$,

$$\bar{U}_i = \tfrac{1}{2}q_-^2(U_{i-1} - U_i) + \tfrac{1}{2}q_+^2(U_{i+1} - U_i) + (q_+ + q_-)U_i + f_i\,\Delta t, \quad (18)$$

with

$$q_\pm = (\tfrac{1}{2} \mp \varepsilon_i)/(1 \pm (\varepsilon_{i\pm1} - \varepsilon_i)) \quad (19)$$

and

$$\varepsilon_i = v_i\frac{\Delta t}{\Delta x}. \quad (20)$$

To achieve second-order accuracy in time, the sources f and the velocities v are usually defined at the half step $\frac{1}{2}\Delta t$. The explicit form of the coefficients $q_\pm$ as given by (19) can be derived from a simple geometrical picture (see, for instance, Ref. [5–8]). The time step is limited to one-half the Courant–Friedrichs–Lewy (CFL) limit.

Considering the case of a constant velocity field and vanishing sources expression (18) can be split into a term corresponding to the usual three-point centered finite difference representation of the continuity equation (17) and a second term proportional to a finite difference representation of a diffusion term of the form $\eta(\partial^2 U/\partial x^2)$. Neglecting the velocity-dependent term in the diffusion coefficient η, we are left with the expression

$$D_i = \tfrac{1}{8}(\bar{U}_{i+1} - 2\bar{U}_i + \bar{U}_{i-1}). \tag{21}$$

Now D has to be subtracted from $\bar{U}$ in order to obtain the densities at the end of a time step. In this last step a flux limiter is invoked that suppresses the generation of new extrema in the antidiffusion step. This way of performing the antidiffusion step is not the most sophisticated but nevertheless a very effective method.

Retaining the velocity dependent diffusion coefficient for the antidiffusion leads to the "phoenical SHASTA" algorithm [6]. The latest one-dimensional FCT techniques with fourth-order accurate phases and minimum residual diffusion are included in a recently developed code called LCPFCT [8]. It solves generalized continuity equations of the form

$$U_t = -\frac{1}{r^{\alpha-1}}(r^{\alpha-1}Uv)_r - \frac{1}{r^{\alpha-1}}(r^{\alpha-1}D_1)_r + C_2(D_2)_r + D_3, \tag{22}$$

with $\alpha = 1, 2, 3$ for Cartesian, cylindrical, or spherical coordinates, respectively. The computational grid is allowed to move in a restricted way during the course of a calculation. However, in the numerical applications discussed in Section 6 we restrict ourselves to Cartesian coordinates and uniform Eulerian grids.

The LCPFCT formulation of the transport and diffusion step yields an expression similar in structure to the SHASTA algorithm (i.e., a generalized three-point central differencing scheme). However, the diffusion coefficients used in the antidiffusion step are now more general and chosen in such a way as to reduce the phase errors to fourth order. Especially the velocity dependence of these coefficients is kept.

The relativistic generalization of the FCT algorithms differs from the non-relativistic ones in only two respects. The calculation of the rest-frame quantities is done as described in Section 3. In addition, it was found necessary to avoid the generation of cells with $R > E$ or $M > E$. This can be done through a modification of the flux limiting [17], e.g., not to carry out the antidiffusion step in the respective cells. The simplest possibility is to readjust E to fulfill the conditions $E \geqslant M$, $E \geqslant R$. Violation of the conservation laws introduced by these modifications is, in all cases we have studied, of the order of the numerical accuracy.

5. THE RELATIVISTIC HLLE METHOD

In recent years alternative approaches have been shown to be very effective in solving the Euler equations of non-relativistic compressible hydrodynamics, named "high resolution schemes" (see, e.g., [13, 18]). These are usually based on upwind schemes which incorporate into the numerical algorithm the direction of the nonlinear wave propagation. This establishes the shock-capturing property. A very simple upwind scheme was discussed by Harten *et al.* [9] and supplemented with a prescription to calculate estimates of signal velocities by Einfeldt [10] (see also Davis [19]). Its relativistic extension, called the relativistic HLLE method, will be discussed in this section. To obtain a second-order accurate method van Leer's MUSCL-approach [12] is used.

The HLLE method is a so-called Godunov-type upwind scheme. In the Godunov method the discretized distributions of the conserved variables mass, momentum, and energy density are assumed to be constant within each grid zone. This defines an initial value problem consisting of a series of local Riemann problems. The information contained in the solution of these Riemann problems can be used to determine the fluxes between grid zones. A new piecewise constant approximation is obtained at the next time level by averaging the local Riemann solutions over the grid zones. The time step has to be limited such that no interaction of neighbouring Riemann solutions will occur (CFL-condition). For the Euler equations with the equation of state of an ideal gas the Riemann problem can be solved exactly by a fixed point iteration. To reduce the computational effort or if the derivation of the solution of the Riemann problem is not possible or too cumbersome, approximate solutions can be used to determine the numerical fluxes of mass, momentum, and energy. Methods based on such an approximate Riemann solution are called Godunov-type schemes.

We start with a formal vector notation of the system of conservation laws (1)–(3)

$$U_t + F(U)_x = 0, \tag{23}$$

where U is the vector of the conserved variables $U = \{R, M, E\}^T$ and $F(U)$ the flux $F(U) = \{Rv, Mv + p, (E + p)v\}^T$. An explicit numerical scheme in conservation form, reproducing the integral conservation properties, is given by

$$U_i^{n+1} = U_i^n - \lambda(G_{i+1/2}^n - G_{i-1/2}^n), \tag{24}$$

with $\lambda = \Delta t/\Delta x$. As usual, Δt is the time step and Δx is the (uniform) step size in space. The superscripts n denote the number of time steps, the indices i define cell centers,

the indices $i \pm 1/2$ the corresponding cell faces. The values $G_{i+1/2}$ are the numerical fluxes between the grid cells,

$$G^n_{i+1/2} = G(U^n_i, U^n_{i+1}), \tag{25}$$

where G is called the numerical flux function.

A first approximation to the Godunov method has been proposed by Roe [20, 21]. He replaced the exact solution of the Riemann problem by that of the Riemann problem for the linearized equation

$$U_t + \bar{A} U_x = 0, \tag{26}$$

where $\bar{A}$ is a special mean value Jacobian matrix $\bar{A} = dF(\bar{U})/d\bar{U}$, the so-called Roe matrix. In the case of an ideal gas an appropriate definition of the average $\bar{U}$ has been given by Roe [20]. The Riemann problem for the linear equation (26) can be solved using the theory of characteristics. But this requires the eigenvalues and eigenvectors of the Jacobian matrix $\bar{A}$. This becomes quite complicated for a relativistic hydrodynamic code with the strong coupling of conservation laws (1)–(3) and the transformation equations (4)–(7) and, in addition, with a complicated equation of state.

It is therefore necessary to use a simpler method. Harten *et al.* [9] showed how to construct a simple approximate Riemann solution. In Roe's method for the Euler equations the exact solution of the Riemann problem, which consists of four constant states separated by elementary waves, is replaced by four constant states separated by linear discontinuities. The Riemann solver of Harten *et al.* contains only three constants states: the approximate Riemann solution has the form

$$U(x, t; U_l, U_r) = \begin{cases} U_l & \text{for} \quad x < b_l t, \\ U_{lr} & \text{for} \quad b_l t \leqslant x \leqslant b_r t, \\ U_r & \text{for} \quad x > b_r t. \end{cases} \tag{27}$$

This construction assumes that we have a priori bounds for the smallest and largest signal velocities b_l and b_r, respectively. U_l and U_r are the unperturbed states on the left and right. The intermediate state U_{lr} is determined by requiring consistency of the approximate Riemann solution (27) with the integral conservation equations over a grid zone. A short calculation gives

$$U_{lr} = \frac{b_r U_r - b_l U_l - F(U_r) + F(U_l)}{b_r - b_l}. \tag{28}$$

The numerical flux associated with (27) and (28) has the form

$$G(U_l, U_r) = \frac{b_r^+ F(U_l) - b_l^- F(U_r) + b_r^+ b_l^- (U_r - U_l)}{b_r^+ - b_l^-}, \tag{29}$$

where

$$b_l^- = \min(0, b_l), \qquad b_r^+ = \max(0, b_r). \tag{30}$$

It is obtained by substituting the Riemann solution into the integral conservation laws over half the grid zone to the left and right of the cell interface.

An essential ingredient of the scheme are good a priori estimates for the smallest and largest signal velocities. In the non-relativistic case Einfeldt [10] proposed calculating them based on the smallest and largest eigenvalues of the Roe matrix. This HLLE scheme is a very robust upwind scheme for the Euler equations. It has been shown in [11] that it is positively conservative, which means that the internal energy and density remain positive throughout the computational process as long as no vacuum will occur in the exact solution. This property is important in regions of highly energetic flows and low densities. The method of Roe does not possess this property (see [11]). On the other hand, introducing only one constant state between the unperturbed regions will increase the numerical dissipation, especially at contact discontinuities. The resolution of single shocks is identical. We note that Einfeldt [10] proposed a modified HLLE scheme, replacing the constant intermediate state by a linear one which reduces the numerical dissipation in the linear degenerate characteristic field. But this method also uses the eigenvectors.

In the relativistic case we define bounds for the signal velocities by the expressions

$$\begin{aligned} b_r &= (\bar{v} + \bar{c}_s)/(1 + \bar{v}\bar{c}_s), \\ b_l &= (\bar{v} - \bar{c}_s)/(1 - \bar{v}\bar{c}_s), \end{aligned} \tag{31}$$

where c_s denotes the relativistic sound velocity and the bar denotes an average of the right and left states. Note that these expressions correspond to relativistic addition (subtraction) of $\bar{v}$ and $\bar{c}_s$ and are thus the natural generalization of the non-relativistic analogue $\bar{v} \pm \bar{c}_s$. For the average in the calculations presented below we use the arithmetic average

$$\bar{v} = (v_l + v_r)/2, \qquad \bar{c}_s = (c_{s,l} + c_{s,r})/2. \tag{32}$$

For weak shocks this is a good approximation of the shock speed up to second-order terms in shock strength. Especially for strong shocks this choice may introduce wiggles. To approximate the proper spreading of the characteristics in the case of a rarefaction wave these simple averages are modified by

$$\begin{aligned} \bar{b}_r &= \max\left(b_r, \frac{v_r + c_{s,r}}{1 + v_r c_{s,r}}\right), \\ \bar{b}_l &= \min\left(b_l, \frac{v_l - c_{s,l}}{1 - v_l c_{s,l}}\right). \end{aligned} \tag{33}$$

In this way the signal velocities for a shock travelling to the left or right are not affected: $\bar{b}_r = b_r$ and $\bar{b}_l = b_l$. For a rarefaction wave this modification prevents the underestimation of the signal velocities and the approximation of unphysical rarefaction shocks. We note that the underestimation of the signal velocities may introduce instabilities or entropy violating shocks, because the numerical domain of dependence does not completely cover that of the exact solution. If we overestimate the signal velocities the scheme remains stable, but the numerical dissipation will be increased. According to the CFL-condition the upper and lower limits for the signal velocities are

$$b_r = 1/\lambda, \qquad b_l = -1/\lambda. \tag{34}$$

The HLLE scheme in conservation form with the numerical flux (29), (30) and the signal velocities (34) is identical to the Lax–Friedrichs scheme [22]. It is well known that this scheme possesses a large amount of numerical dissipation. For relativistic flows we have another possibility for the choice of the signal velocities through a priori estimates for the velocity. The choice

$$b_r = c = 1, \qquad b_l = -c = -1, \tag{35}$$

where c denotes the velocity of light, yields a simple and robust numerical method which is only applicable to highly relativistic flow. Otherwise the numerical dissipation produces very crude results.

Another method of calculating the averaged signal velocities that was tried was inspired by Roe's non-relativistic formulae

$$\begin{aligned} \tilde{v} &= \frac{\sqrt{R_r}\, v_r + \sqrt{R_l}\, v_l}{\sqrt{R_r} + \sqrt{R_l}} \\ \tilde{c}_s^2 &= \frac{\sqrt{R_r}\, c_{s,r}^2 + \sqrt{R_l}\, c_{s,l}^2}{\sqrt{R_r} + \sqrt{R_l}} \\ &\quad + \frac{\Gamma - 1}{2} \frac{\sqrt{R_r R_l}}{(\sqrt{R_r} + \sqrt{R_l})^2} (v_r - v_l)^2. \end{aligned} \tag{36}$$

In our test problems we found only minor differences to Eq. (32), only for the special case of $c_s \simeq 0$ is Eq. (36) to be preferred (see below).

The equation for the numerical flux (29) and (30), together with the definition of the signal velocities (33), defines our first-order relativistic HLLE algorithm. To achieve second-order accuracy we use the MUSCL-approach introduced by van Leer [12] (see also [23]). Van Leer replaced Godunov's piecewise constant distribution by a piecewise linear one. That means that, in a first step, slopes are calculated in each grid zone. This is to be done by a monotonicity-preserving interpolation of the integral approximative values. These slopes define right and left boundary values in each grid zone. Second order in time is achieved by updating these boundary values after half a time step. Here we only approximate the change of the piecewise linear distribution inside the cell. New approximative integral values on the next time level are now obtained by the scheme in conservation form (27), where the flux between the grid zones is calculated by the relativistic HLLE flux (29), (30), and (33), but now using the updated boundary values within the grid zones instead of the integral values in the first-order method. A detailed listing of the second-order relativistic HLLE algorithm is given in the Appendix. For simplicity we will call this second-order version also relativistic HLLE. We do not show any results of the first-order scheme.

In recent years a number of appropriate slope calculations for the first step within the MUSCL-type scheme has been proposed; a review is given in [24]. These slope calculations guarantee, e.g., the preservation of monotonicity or the TVD-property (total variation diminishing). In this paper we use the simplest slope prescription as given by Roe (see [24]). If a_i and b_i denote the right- and left-hand difference quotient of the vector U in the ith grid zone, then the vector of slopes S_i is determined by the formula

$$S_i = \operatorname{minmod}(a_i, b_i) = \begin{cases} a_i & \text{for } |a_i| \leqslant |b_i|,\ a_i \cdot b_i > 0, \\ b_i & \text{for } |a_i| > |b_i|,\ a_i \cdot b_i > 0, \\ 0 & \text{otherwise.} \end{cases} \tag{37}$$

The piecewise linear approximations need not necessarily be defined in the conserved quantities U. In non-relativistic calculations best results for a MUSCL-type scheme are usually obtained using characteristic variables. This is based on Roe's [20] local linearization of the nonlinear system, which defines a local system of characteristic fields. This method, however, again requires the knowledge of the eigenvectors of the Roe matrix. Another possibility is the use of the primitive variables n, p, and v to perform the slope approximation. This method has the advantage that step 2 of the relativistic HLLE algorithm (see Appendix) is superfluous. This alternative approach has been tested replacing the variable v by the expression γv to get a better resolution in the case of ultra-relativistic velocities. In most of the test cases in the next section only insignificant differences between these two methods occur. In general, the use of primitive variables in the slope calculation leads to larger numerical viscosity. This improves the stability of the algorithm, especially for shock tube problems with strong initial pressure gradients.

6. SAMPLE PROBLEMS AND TEST CALCULATIONS

6.1. *The Shock Tube Problem and the One-Dimensional Shock Model*

For validation and comparison we apply the numerical algorithms to relativistic Riemann problems which admit an analytical solution or a solution by numerical integration of an ordinary first-order differential equation, as will be summarized below. Our first test problem is a flow in a shock tube at relativistic velocities. At time $t=0$ two regions of fluid with pressures p_0 and p_4 and densities n_0 and n_4, respectively, are separated by a diaphragm. For a shock tube problem the velocities on both sides are zero. At $t=0$ this diaphragm is suddenly removed. Identically to the non-relativistic case four constant states occur separated by three elementary waves: either shock waves or rarefaction waves and a contact discontinuity. We consider a shock tube problem for which the solution has the following structure: a rarefaction wave travels to the left and a shock wave to the right, followed by a contact discontinuity. This situation is sketched in Fig. 1. We denote the different states by numbers 0 to 4. Regions 0 and 4 are the undisturbed fluid still at rest, region 1 is the rarefaction fan, region 2 is the constant state between the tail of the rarefaction wave and the contact discontinuity, while region 3 is the shock plateau.

The solution of the Riemann problem is obtained by matching pressure and velocity at the rarefaction tail and at the shock front, i.e., by the requirement

$$p_2 = p_3, \qquad v_2 = v_3. \tag{38}$$

The rarefaction wave can be determined by applying similarity methods, as discussed in detail in Ref. [25] for the equation of state (8). This requires the numerical integration of an ordinary first-order differential equation,

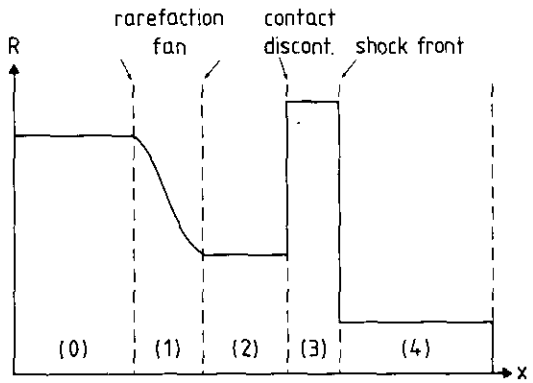

FIG. 1. Schematic representation of the density profile in the shock tube problem. Five regions can be identified: the undisturbed fluid (0) and (4), the rarefaction fan (1), the region bounded by the rarefaction tail and the contact discontinuity (2), and the shock plateau bounded by the contact discontinuity and the shock front (3).

as will be summarized below. If instead the ultra-relativistic limit (9) is assumed, this problem can be solved analytically.

In solving the relativistic isentropic expansion, the mass and momentum equations (1) and (2) are used. The energy equation (3) is replaced by the adiabatic expansion law

$$(e-n)/(e_0-n_0) = (n/n_0)^{\Gamma}. \tag{39}$$

Note that $\gamma_0 \equiv 1$. The index 1 has been dropped. The pressure can be eliminated in the momentum equation by means of relations (8) and (39).

Defining the similarity variable

$$\zeta = x/t \tag{40}$$

the continuity equation can be written in the form

$$\frac{dR}{dv} = -\frac{R}{v-\zeta}. \tag{41}$$

Using the definition of the energy-momentum tensor, the equation of state and the quantity $B \equiv \gamma(e-n)$ the momentum can be expressed by

$$M = (R + \Gamma B)\,\gamma v. \tag{42}$$

Calculating the total derivatives $dR/d\zeta$ and $dv/d\zeta$ we are left, after some algebraic manipulations, with the ordinary first-order differential equation

$$\frac{dR}{dv} = \frac{R}{1-v^2}\left(v - \sqrt{\frac{R+\Gamma B}{\Gamma(\Gamma-1)B}}\right). \tag{43}$$

Note that there is an error in the corresponding formula (C.13) of Ref. [25]. Equation (43) is integrated using a fourth-order variable step Runge–Kutta procedure starting with $v^{(0)} = 0$.

The solution of the relativistic shock wave is given by the Rankine–Hugoniot–Taub relations [26]. In the laboratory system (rest frame of fluids 0 and 4) the following relations hold:

$$v_3 = \left[\frac{(p_3-p_4)(e_3-e_4)}{(e_4+p_3)(e_3+p_4)}\right]^{1/2} \tag{44}$$

$$v_{\text{shock}} = \left[\frac{(p_3-p_4)(e_3+p_4)}{(e_4+p_3)(e_3-e_4)}\right]^{1/2}. \tag{45}$$

The last two relations can be combined yielding

$$v_{\text{shock}} = \frac{1}{v_3}\frac{p_3-p_4}{e_4+p_3}. \tag{46}$$

The compression ratio is determined by the relation

$$\frac{n_3}{n_4}=\frac{\tilde{\gamma}_4\tilde{v}_4}{\tilde{\gamma}_3\tilde{v}_3}, \tag{47}$$

where the tilde denotes quantities defined in the rest frame of the shock front.

The solution of the relativistic Riemann problem is now obtained by matching $p^{(i)}$ and $v^{(i)}$, the pressure and velocity of the ith integration step in solving Eq. (43), with p_3 and v_3. The code can be made more efficient by first solving Eq. (46) for $v_3=v^{(i)}$. As long as the resulting shock velocity exceeds the speed of light the guess yields unphysical results and no complete solution of the Taub relations has to be provided. As soon as $v_{\text{shock}}\leqslant 1$ the relativistic jump conditions are solved and the quantity

$$p_4^{(i)}=(e_3+p_3)\,\tilde{v}_3\tilde{\gamma}_3^2(\tilde{v}_3-\tilde{v}_4)+p_3 \tag{48}$$

is calculated. The matching condition now reads

$$|p_4^{(i)}-p_4|<\varepsilon. \tag{49}$$

Initially the difference in (49) is negative. As soon as it becomes positive, the final solution is obtained by a regula falsi procedure.

In the ultra-relativistic limit of the ideal gas equation of state (9), the solution of the Riemann problem can be simplified considerably. Because B is proportional to the internal energy a consistent treatment of the ultra-relativistic limit also requires the limit $n\to 0$ in the definition of B, i.e., $B=\gamma e$. This yields the ultra-relativistic limit of Eq. (43)

$$\frac{dR}{dv}=\frac{R}{1-v^2}\,[v-(\Gamma-1)^{-1/2}] \tag{50}$$

which may be solved analytically,

$$\ln R=\ln R_0-\tfrac{1}{2}\,[\ln(1-v^2)+(\Gamma-1)^{-1/2}\ln((1+v)/(1-v))]. \tag{51}$$

The relativistic jump conditions can also be simplified in the case of Eq. (9), yielding a simple quadratic form for the pressure p_3,

$$p_3^2(v_3^2-1)+p_3\,p_4(v_3^2/(\Gamma-1)+v_3^2(\Gamma-1)+2)+p_4^2(v_3^2-1)=0. \tag{52}$$

Solutions of the relativistic Riemann problem are discussed, together with the numerical test runs, in Subsection 6.2.

The second test problem is another Riemann problem, the one-dimensional shock model proposed in [27]. Because it offers an analytical approach to the physics of shock waves it is useful in order to obtain estimates of equation of state effects in relativistic heavy ion collisions [28].

In the one-dimensional shock model in its simplest form two identical slabs of matter collide (see Fig. 2). Initially there is a uniform distribution of density and energy, $n_{\text{left}}=n_{\text{right}}=n_0$ and $e_{\text{left}}=e_{\text{right}}=e_0$, while $v_{\text{left}}=v>0$ and $v_{\text{right}}=-v$. This defines the two slabs touching at $t=0$. For $t>0$ the matter in the collision zone is compressed yielding values $n>n_0$ and $e>e_0$. If the absolute values of the incoming velocities exceed the local speed of sound two shock waves are generated travelling in opposite directions into the inflowing matter. This problem is thus similar to the wall shock problem frequently used as a test case in numerical hydrodynamics (see, e.e., [4, 25, 29]). The one-dimensional shock model corresponds to the wall shock problem reflected at the fixed boundary. The solution of the one-dimensional shock model is given by the Rankine–Hugoniot–Taub relations discussed above.

One important special case is the shock heating of a cold fluid defined by $p_0=0$. In this case the compression ratio $\sigma=n/n_0$ is given by the relation ($\gamma\equiv e/n$)

$$\sigma=\frac{\Gamma+1}{\Gamma-1}+\frac{\Gamma}{\Gamma-1}\,(\gamma-1),\ \gamma>1. \tag{53}$$

6.2. *Test Runs*

The main differences between relativistic and non-relativistic Riemann problems are due to the non-linear velocity addition and the Lorentz contraction. The first effect yields a curved velocity profile for the rarefaction fan, whereas in the classical case there is a linear profile. The Lorentz contraction narrows the shock plateau and allows the classical ideal gas limit of $(\Gamma+1)/(\Gamma-1)$ for the compression ratio at the shock front to exceed, as is indicated by Eq. (53) for the strong shock limit. These effects become particularly strong in the ultra-relativistic case. Also the rarefaction fan can become squeezed considerably if the velocity of sound c_s approaches the speed of light, i.e., $\Gamma\to 2$ and $e\gg n$ in the Appendix, Eq. (3).

The first setup for the numerical test runs is a mildly relativistic shock tube with $n_0=1$, $n_4=0.125$ and $p_0=1$, $p_4=0.1$. Equation of state (8) is applied with $\Gamma=1.4$. The structures of the resulting profiles are quite similar to the

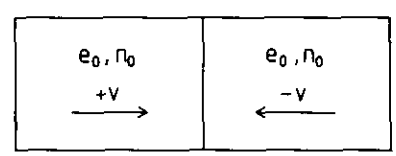

FIG. 2. Initial configuration of the one-dimensional shock model. Two identical slabs of matter are colliding with opposite velocities v and $-v$. They are just touching at $t=0$.

non-relativistic case, for which it is a standard benchmark and usually called Sod's problem [30]. In Fig. 3 the pressure p, the velocity v, and the proper density R are shown for the relativistic HLLE, phoenical SHASTA, and LCPFCT algorithm, respectively. Obviously relativistic HLLE produces the best results. The absolute value of the various plateaus is reproduced very well without numerical oscillations. In contrast, both SHASTA and LCPFCT show numerical oscillations that are particularly strong in the region between rarefaction tail and contact discontinuity. In addition to these long wavelength oscillations, in the LCPFCT run there are overshoots and undershoots restricted to one cell just at the contact discontinuity and the shock front, respectively. Those are best visible in the velocity profile.

However, due to the antidiffusion step the FCT algorithms are able to produce sharper profiles of the discontinuities. So the shock fronts in the SHASTA and LCPFCT are much narrower than in the relativistic HLLE calculation. One can observe this directly in Fig. 3 comparing the number of grid points over which the shock fronts extend.

The results of Fig. 3 can be compared to calculations described in [4], in which the same Riemann problem was used as a test case for a fully implicit one-dimensional relativistic hydrodynamic code. Results for three different types of computational meshs are discussed, with a total number of 200 grid points in each case. Using an Eulerian grid there is a broad overshoot at the transition region between rarefaction wave and contact discontinuity. The width of the shock front is nine zones. In the Lagrangian

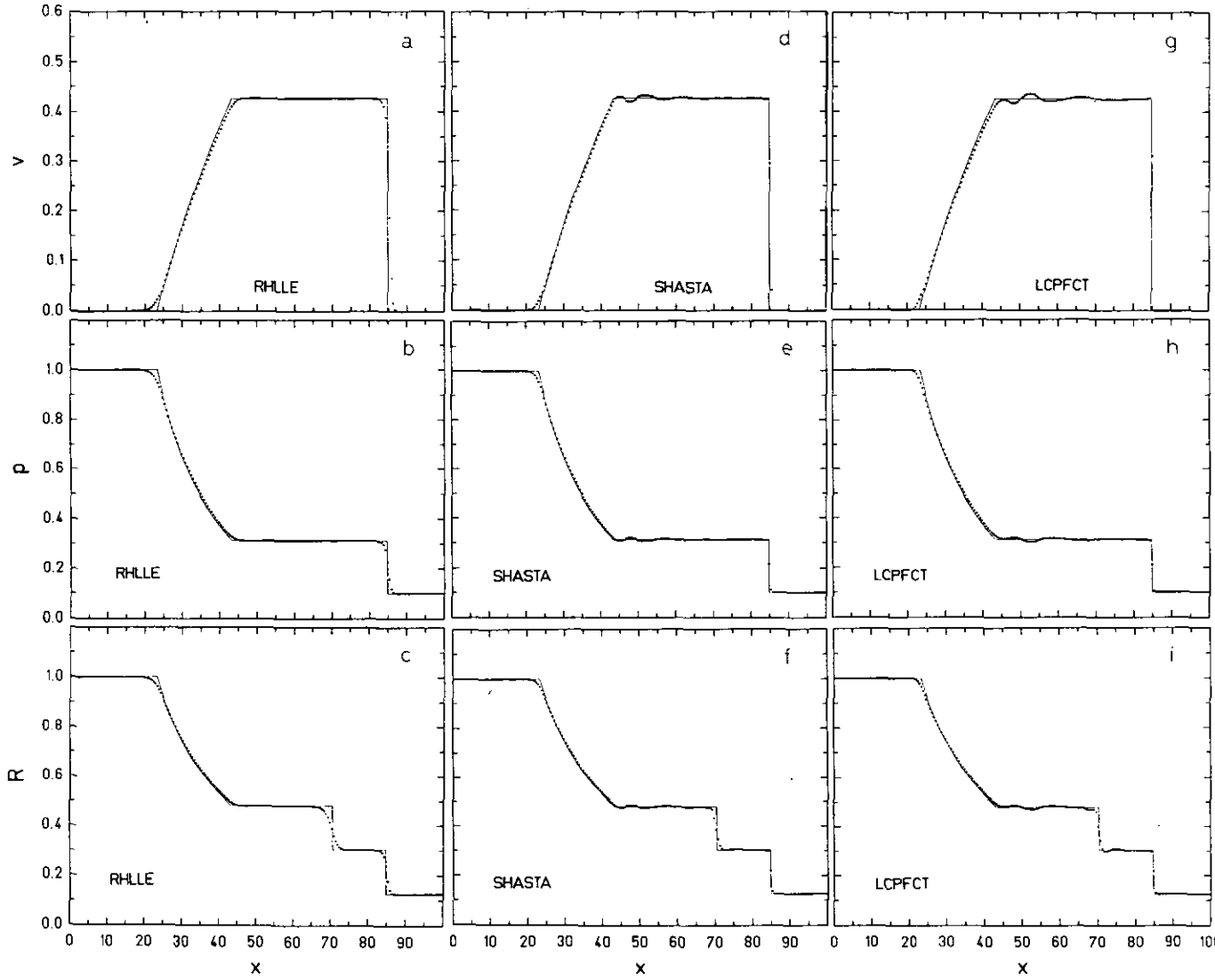

FIG. 3. The shock tube problem for time $t = 48$ on a 200-zone mesh with $\Delta t = \Delta x/3$. In all figures the full line corresponds to the exact solution: (a) velocity; (b) pressure; (c) proper density profile, calculated with the relativistic HLLE algorithm; (d–f) the same quantities calculated with the SHASTA algorithm; (g–i) calculated with the LCPFCT algorithm.

calculation this overshoot is still present; however, it is somewhat smaller. The shock front now spreads over 13 zones that, of course, now have a smaller Δx so that the absolute width of the shock is reduced. Good results are obtained only in the adaptive mesh calculations. In this case the grid points are extremely concentrated at locations showing gradients in the mass, momentum, or energy density, allowing an accurate reproduction of the shock tube profiles.

The second test case is a Riemann problem including the shock heating of a cold fluid (Fig. 4). The initial conditions are now $p_0 = 13\frac{1}{3}$, $p_4 = 0$ ($p_4 = \frac{2}{3} \times 10^{-6}$ numerically) and $n_0 = 10$, $n_4 = 1$ with $\Gamma = \frac{5}{3}$ in Eq. (8).

The fluid velocity now slightly exceeds 0.7 and, thus, the relativistic effects are much more pronounced than in the previous problem. The extreme pressure gradient establishes a tough test case for any algorithm. Thus relativistic HLLE, SHASTA, and LCPFCT show deviations from the exact solutions. The best agreement with the analytical result is again obtained with the relativistic HLLE algorithm. Besides a small oscillation on the contact discontinuity plateau near the rarefaction fan, the only considerable deviation from the analytical solution is the shape and height of the shock plateau in the density distribution. The LCPFCT algorithm shows similar results; however, the quality of reproduction of the plateau values is slightly worse than in the HLLE code. Again, the most severe deviation is found at the shock plateau density. Relativistic HLLE and LCPFCT underestimate this density by about 10%. SHASTA, on the other hand, produces a much too

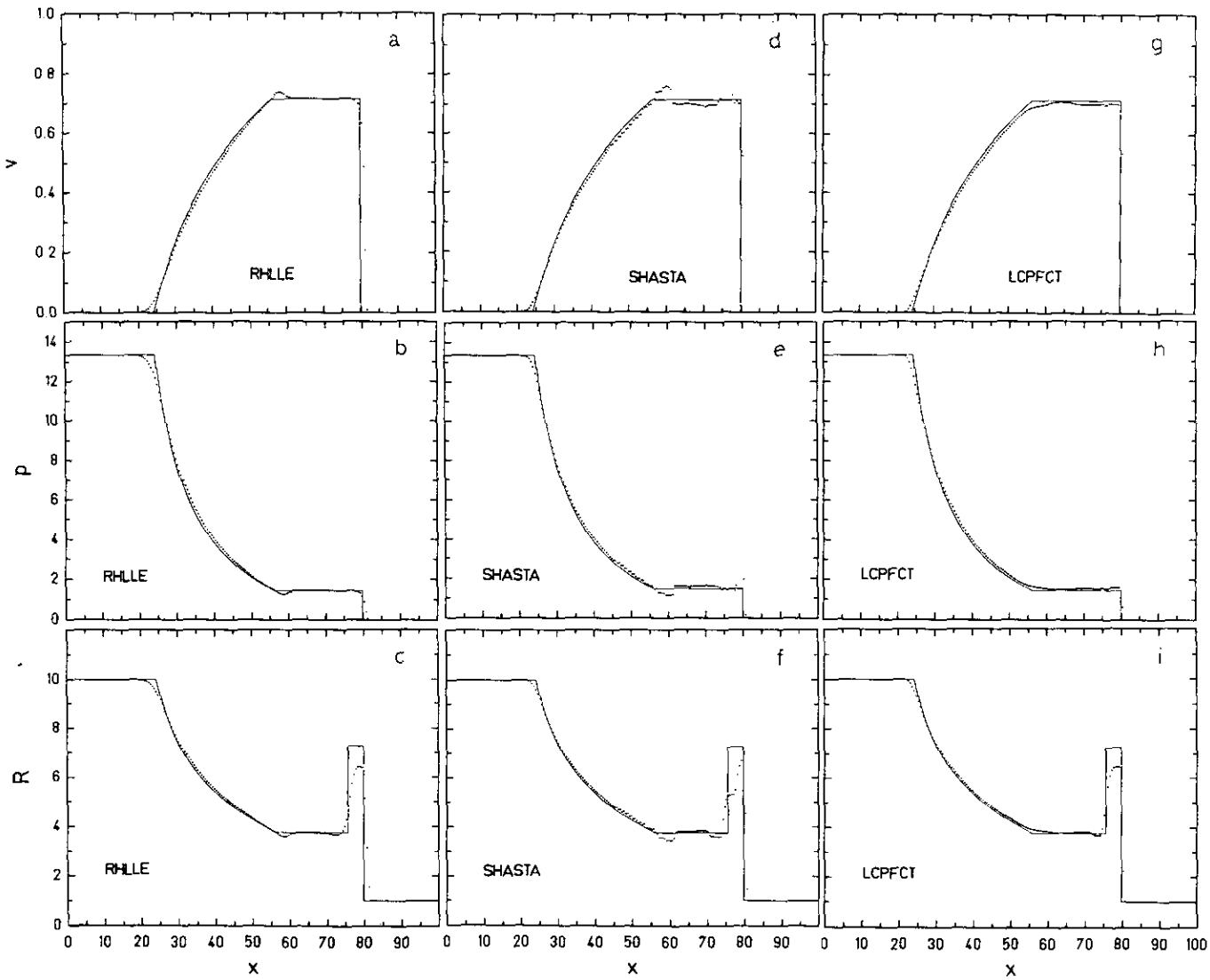

FIG. 4. The shock tube problem for time $t = 36$ on a 200-zone mesh with $\Delta t = \Delta x/5$: (a–c) velocity, pressure, and proper density profile, calculated with the relativistic HLLE algorithm; (d–f) the respective quantities calculated with the SHASTA; (g–i) the quantities calculated with the LCPFCT algorithm.

low density plateau with a spike at the shock front. Also the oscillatoric behaviour at the tail of the rarefaction fan is more pronounced than in the other algorithms.

Similar results are obtained by Centrella and Wilson in Ref. [25]. The density shock plateau in their calculations is, however, reduced to a peak that may be an artefact of an overshoot in the pressure distribution. This distribution, however, is not shown in the respective reference.

A Riemann problem including the ultra-relativistic equation of state (9) with $\Gamma = 1.99$ is studied in Fig. 5. The initial conditions are $p_0 = 1990$, $p_4 = 995$, $n_0 = 2$, $n_4 = 1$. The velocity of sound then has a constant value of 0.995, yielding a box-like shape of the velocity profile, as discussed above.

Again there is a nice correspondence between exact solution and relativistic HLLE. Only in the density profile at the shock plateau are there very small oscillations, whereas the density plateau between the rarefaction fan and the contact discontinuity, as well as the pressure and velocity plateaus, are nearly perfectly uniform.

On the other hand, there are strong overshoots in the velocity profile calculated with LCPFCT and SHASTA, yielding corresponding undershoots and overshoots in pressure and density. This shows that highly relativistic sound velocities can cause numerical problems even in weak shock tube problems with initial pressure and density ratios of only 2. This is important because, in future applications using nuclear matter equations of state, sound velocities close to the speed of light could be possible [28].

A comparison of the results produced by relativistic HLLE, LCPFCT, and SHASTA for colliding slabs is shown in Fig. 6. The straight line is the analytical result obtained from the one-dimensional shock model discussed above.

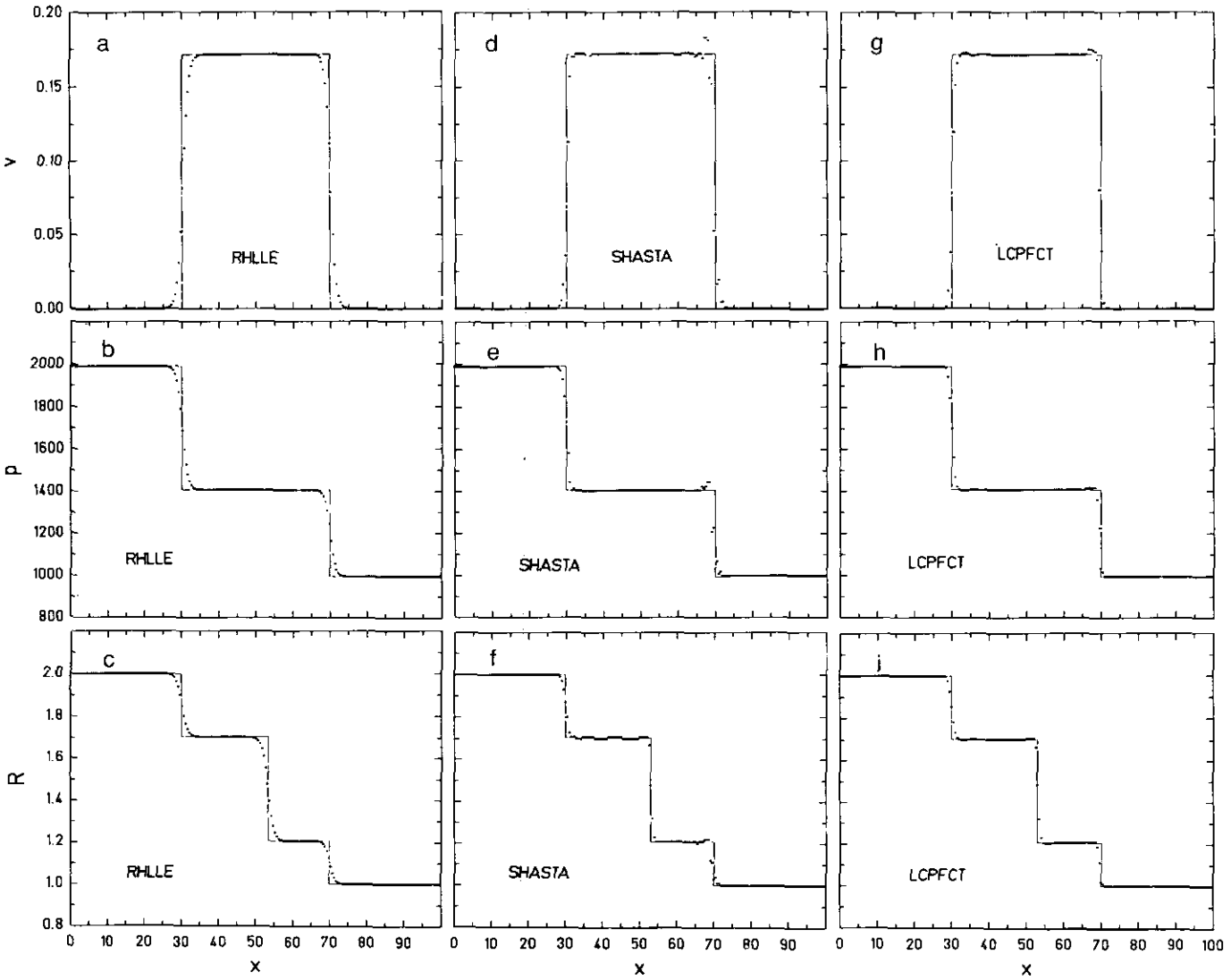

FIG. 5. The shock tube problem for time $t = 20$ on a 200-zone mesh with $\Delta t = \Delta x/3$: (a–c) velocity, pressure, and proper density profile, calculated with the relativistic HLLE algorithm; (d–f) the same quantities, calculated with the SHASTA; (g–i) the quantities calculated with the LCPFCT algorithm.

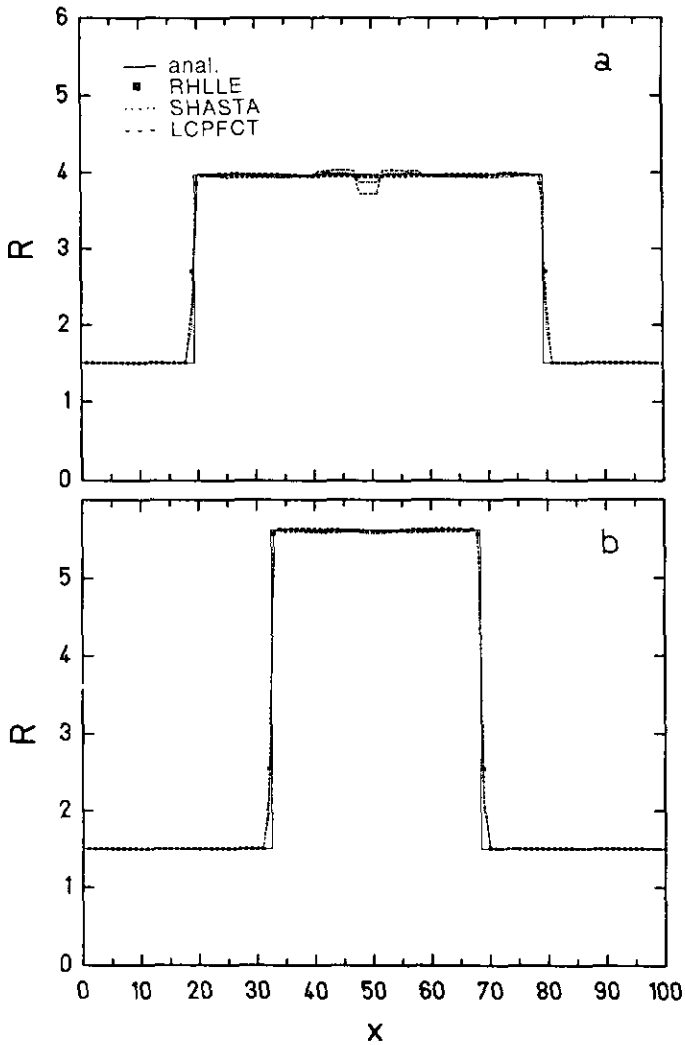

FIG. 6. Proper density profile of a one-dimensional shock model calculation with $\gamma = 10$ and $e_0 = n_0 = 0.15$, after 150 iterations with $\Delta t = \Delta x/3$ on a 100-zone mesh. The equation of state is $p = (\Gamma - 1)(e - n)$: (a) $\Gamma = \frac{5}{3}$; (b) $\Gamma = 1.4$.

Again relativistic HLLE is clearly closest to the exact solution. There is only a slight dip in the central region of the shocked matter. For $\Gamma = \frac{5}{3}$ (Fig. 6a) LCPFCT and SHASTA exhibit numerical oscillations around the uniform solution with a pronounced undershoot in the central region. These oscillations are closely related to the value of the adiabatic index or the type of equation of state applied. They are reduced if we take $\Gamma = 1.4$ and otherwise unchanged initial conditions (cf. Fig. 6b) or if we use the ultra-relativistic equation of state $p = (\Gamma - 1)e$, instead of $p = (\Gamma - 1)(e - n)$. The width of the shock front is two zones for all three algorithms.

Figure 6 shows the situation for colliding slabs after a comparatively long period of time. This is contrasted with Fig. 7, showing a colliding slab run with half the number of grid points and after a much shorter period of time. This

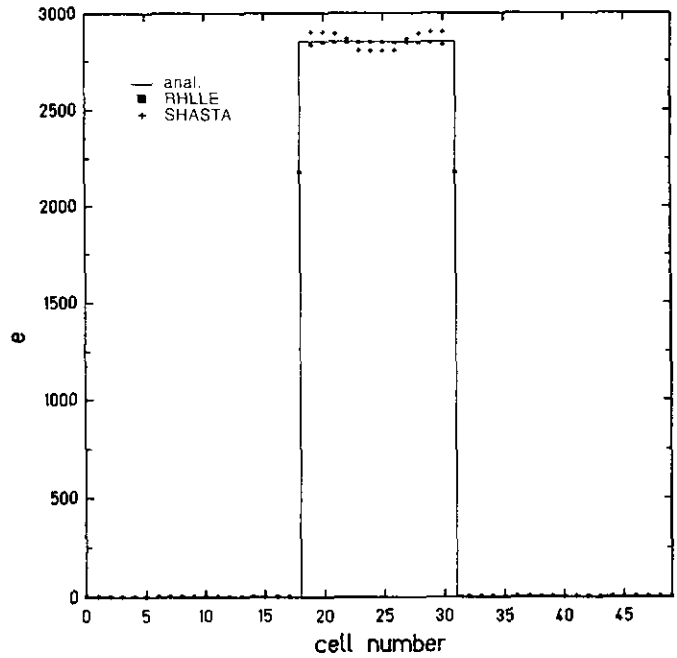

FIG. 7. Rest frame energy e profile of a one-dimensional shock model calculation with $\gamma = 10.37$ and $e_0 = 5$, $n_0 = 2$, after 100 iterations with $\Delta t = \Delta x/5$ on a 50-zone mesh. $p = e/3$ has been assumed.

tests the ability of the code to fulfil the conservation relations locally even during the early stages of the collision. SHASTA produces long wavelength oscillations around the exact solution that are only reduced with increasing time, while relativistic HLLE establishes the energy plateau correctly from the very beginning. Other explicit relativistic hydrodynamic codes usually show strong limitations in the allowed γ-factors [25, 29].

Figure 8a shows the energy e for a $\gamma = 10^6$ collision. Even on the logarithmic scale the analytic solution is reproduced perfectly. The shock width is only one zone. The same problem calculated with SHASTA (Fig. 8b) also gives the correct plateau, however, with a very broad and irregular shock front. The results for LCPFCT are quantitatively similar with those obtained by SHASTA.

The shock heating of a cold fluid has been used as a test case for the transport algorithm in [4, 25, 29]. Wall shock boundary conditions are assumed in those calculations. Figure 9 compares the relative error in the compression ratio for the relativistic HLLE, SHASTA, and LCPFCT codes with results given in Ref. [29]. In the case of relativistic HLLE, SHASTA and LCPFCT the one-dimensional shock model has been assumed to provide the boundary conditions. A 100-zone grid has been used. As discussed above, the physical solution is identical to the (reflected) wall shock problem but the numerical simulation is somewhat more difficult in the one-dimensional shock model case. The initial conditions are $n_0 = 1$ and $e_0 = 1$ ($e_0 = 1.000001$ numerically) and $\Gamma = \frac{5}{3}$ in equation of state

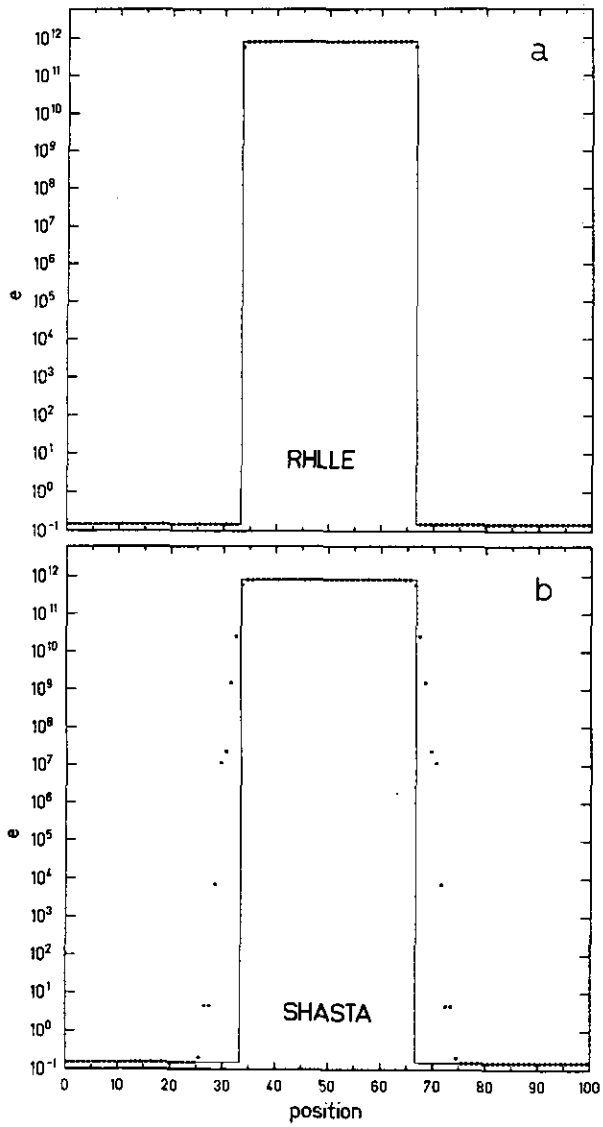

FIG. 8. Rest frame energy e profile of a one-dimensional shock model calculation with $\gamma = 10^6$ and $e_0 = n_0 = 0.15$, after 150 iterations with $\Delta t = \Delta x/3$ on a 100-zone mesh. The full line is the analytical result, $p = e/3$ has been assumed: (a) the relativistic HLLE results; (b) the SHASTA results.

(8); γ is varied between 1.5 and 50. The relative error is obtained by first calculating the average in the density $\bar{n}$ over the plateau of shocked matter, with an assumed shock width of two zones, and then calculating the quantity $(\bar{n} - n_{\text{theory}})/n_{\text{theory}}$. This definition has been taken over from Ref. [25].

The results cited in [29] (where an improved version of the code discussed in [25] was applied) show a strong γ-dependence with a relative error $> 2\%$ for $\gamma > 7$. In the LCPFCT, SHASTA, and relativistic HLLE results there is no such strong increase in error with increasing γ. For LCPFCT and SHASTA the relative error for $\gamma \geqslant 10$ is about 0.5%; for relativistic HLLE it is only 0.2%.

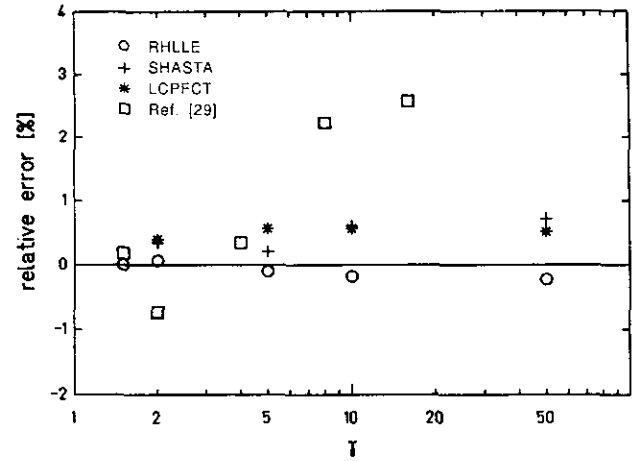

FIG. 9. Relative error in the compression ratio obtained by several numerical algorithms in a shock heating of cold fluid simulation.

Furthermore, a strong Γ-dependence of the transport algorithm was found in [25] while a test calculation using relativistic HLLE with $\gamma = 10$ and $\Gamma = \frac{4}{3}$ yields exactly the same relative error as for $\Gamma = \frac{5}{3}$.

In [4] the same wall shock problem was calculated using the implicit algorithm on an Eulerian grid with 200 zones, that is, an effective vertex number a factor of 4 larger than in the relativistic HLLE calculations. For $\gamma = 10$ a relative error of 0.2% is stated, compared with 0.18% in the relativistic HLLE calculation.

The slight increase in the relative error with increasing γ in the relativistic HLLE results is due to the definition of the relative error given above. For small values of γ there are small oscillations around the exact value n_{theory} that cancel in performing the average over the shock plateau, while for $\gamma > 10$ the code value is systematically too low. If, instead, the variance were calculated, the error would be nearly constant at about 0.2%.

In some of the test problems, using equation of state (8), regions occur in which the sound velocity c_s approaches zero (which can be physically reasonable for some model calculations of nuclear matter). This leads to spurious oscillations near the shock in relativistic HLLE, if Eq. (32) is used to calculate the signal velocities. One may use Roe's prescription of the signal velocities (36); alternatively, a simple numerical fix was employed: the signal velocities were required to exceed a cutoff value δ in magnitude; $\delta \simeq 5 \times 10^{-4}$ was found to yield satisfactory results.

6.3. *Conclusion*

In this paper we were able to compare one-dimensional test problems solved with the newly developed relativistic HLLE code, a relativistic implementation of the LCPFCT algorithm, the well-established relativistic version of phoenical SHASTA, the explicit code described in [25, 29],

and the implicit algorithm discussed in [4]. Restricting our considerations to Eulerian grids due to the demands of future three-dimensional applications, relativistic HLLE yields the best results. It is astonishing that this physically motivated explicit technique is even superior to implicit schemes. Particularly important is the fact that there is practically no restriction for the allowed γ factors. Thus, ultra-relativistic three-dimensional calculations should be possible, using relativistic HLLE and directional splitting techniques.

LCPFCT and phoenical SHASTA, though somewhat less accurate, also do not show the strong γ-dependence that can be found in the codes of [25, 29]. The advantage of the sharper shock profiles in the numerical solution of a Riemann problem due to the antidiffusion step is paid for with numerical oscillations. In the one-dimensional shock model the shock width is identical for relativistic HLLE, LCPFCT, and SHASTA, at least for small and medium γ factors, while for large γ factors there is again a strong advantage for the relativistic HLLE algorithm. This is due to the excellent conservation properties of relativistic HLLE that become particularly important at ultra-relativistic velocities. A more serious problem may be the fact, that, in contrast to relativistic HLLE, it takes some time for LCPFCT and SHASTA to establish the correct stationary solution. This could be of particular importance in ultra-relativistic heavy ion collisions where the compression phase evolves very quickly.

APPENDIX: COMPLETE LISTING OF THE RELATIVISTIC HLLE METHOD

At the beginning of a new computational cycle a complete set of hydrodynamic quantities at time step n is assumed to be known. Remember that R, M, and E are considered to be elements of a vector U and the corresponding fluxes are elements of a vector F. This will allow us to use a symbolical vector notation.

- *Step* 1. *Determination of cell face values.*

$$U^n_{i\pm} = U^n_i \pm \frac{\Delta x}{2} S^n_i, \tag{1}$$

with S^n_i a slope vector as defined in Eq. (37).

Note that now for each cell i a set of three distinct values for all hydrodynamic variables has to be determined: U_i (at cell center i), U_{i+} (at cell face $(i+\frac{1}{2})$) and U_{i-} (at cell face $(i-\frac{1}{2})$, see Fig. 10). The second index $\pm$ is necessary because cell face $(i+\frac{1}{2})$ is common to cell i and cell $(i+1)$. In fact there are only two independent variables, the variable defined at the cell center and the corresponding slope, but in order to increase computational efficiency, the three quantities are stored.

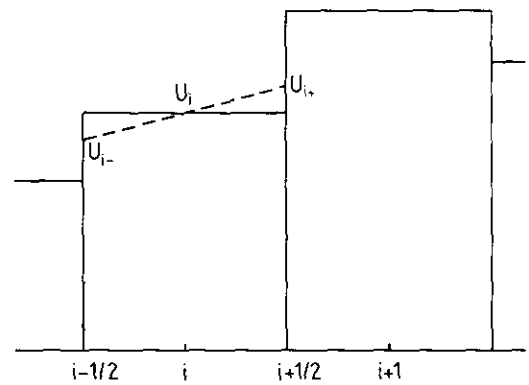

FIG. 10. Definition of the piecewise linear discretization used in the second-order relativistic HLLE method.

- *Step* 2. *Calculation of the rest-frame quantities.* Calculate the rest-frame variables $n_{i\pm}$, $e_{i\pm}$, $p_{i\pm}$, as well as $\gamma_{i\pm}$ and $v_{i\pm}$ corresponding to the Step 1 quantities $U^n_{i\pm}$ (see Section 3).

- *Step* 3. *Updating of the lab-frame quantities for the half time step*:

$$U^{n+1/2}_{i\pm} = U^n_{i\pm} - \frac{1}{2}\frac{\Delta t}{\Delta x}\begin{cases} R^n_{i+}v^n_{i+} - R^n_{i-}v^n_{-} \\ M^n_{i+}v^n_{i+} + p^n_{i+} - M^n_{i-}v^n_{i-} - p^n_{i-} \\ (E^n_{i+} + p^n_{i+})\,v^n_{i+} - (E^n_{i-} + p^n_{i-})\,v^n_{i-}. \end{cases} \tag{2}$$

- *Step* 4. *Calculation of the rest-frame quantities for the half step.* Calculate the rest-frame variables $n_{i\pm}$, $e_{i\pm}$, $p_{i\pm}$ as well as $\gamma_{i\pm}$ and $v_{i\pm}$ at the cell faces $i\pm\frac{1}{2}$ for time step $n+\frac{1}{2}$ (see Section 3).

Steps 3 and 4 provide second-order accuracy in time. Now the first-order relativistic HLLE upwind scheme can be applied on the complete set of variables $U^{n+1/2}_{i\pm}$ and $q^{n+1/2}_{i\pm}$, q being a symbol for the quantities n, e, v, γ, and p.

- *Step* 5. *Calculation of the sound velocity* c_s. The relativistic isentropic sound speed corresponding to the equation of state (8) is given by the relation [25]

$$(c_s)^2 = \frac{\Gamma(\Gamma-1)(e-n)}{n+\Gamma(e-n)}. \tag{3}$$

In the limit $n \to 0$ this equation reduces to the well-known relation $(c_s)^2 = \frac{1}{3}$ in the case of the ultra-relativistic equation of state (9) with $\Gamma = \frac{4}{3}$; c_s has to be calculated at the cell interfaces.

• *Step 6. Estimate of the signal velocities.* It is necessary to define appropriate mean values in calculating the signal velocities from $c_{s,i\pm}^{n+1/2}$ and $v_{i\pm}^{n+1/2}$. If the average is defined by the arithmetic mean, it has to be decided whether first to calculate the mean values of c_s and v and then the signal velocities or vice versa. In special relativity, in contrast to the classical case, the two ways yield different results. The correct procedure, as shown below, is to first calculate the mean values of v and c_s and then the signal velocities. The relations used in the code are (for the arithmetic average)

$$v_{i+1/2}^{n+1/2} = \tfrac{1}{2}(v_{i+}^{n+1/2} + v_{(i+1)-}^{n+1/2}) \tag{4}$$

and

$$c_{s,i+1/2}^{n+1/2} = \tfrac{1}{2}(c_{s,i+}^{n+1/2} + c_{s,(i+1)-}^{n+1/2}). \tag{5}$$

Now the signal velocities can be derived using

$$b_{i+1/2}^{+} = \max\left(0, \frac{v_{i+1/2}^{n+1/2} + c_{s,i+1/2}^{n+1/2}}{1 + v_{i+1/2}^{n+1/2} c_{s,i+1/2}^{n+1/2}}, \frac{v_{(i+1)-}^{n+1/2} + c_{s,(i+1)-}^{n+1/2}}{1 + v_{(i+1)-}^{n+1/2} c_{s,(i+1)-}^{n+1/2}}\right), \tag{6}$$

$$b_{i+1/2}^{-} = \min\left(0, \frac{v_{i+1/2}^{n+1/2} - c_{s,i+1/2}^{n+1/2}}{1 - v_{i+1/2}^{n+1/2} c_{s,i+1/2}^{n+1/2}}, \frac{v_{i+}^{n+1/2} - c_{s,i+}^{n+1/2}}{1 - v_{i+}^{n+1/2} c_{s,i+}^{n+1/2}}\right). \tag{7}$$

That this prescription is the correct one in calculating mean values of signal velocities can be seen from the test problem of two colliding slabs of equal e and n but opposite sign of v touching at $t=0$ at cell face $k+\frac{1}{2}$ (see Section 6). Using the method described above, the algorithm reproduces the correct physical behaviour; that is, at first the density in cells k and $k+1$ increases while the corresponding absolute value of the velocities decreases. As soon as the density limit prescribed by the Rankine–Hugoniot–Taub relations is reached, the velocities associated with cells k and $k+1$ are about zero and cells $k-1$ and $k+2$ are now subject to compression and so on, thus describing two shock waves propagating in opposite directions. This can be achieved because Eq. (4) yields a mean value of $v=0$ at cell face $k+\frac{1}{2}$.

On the other hand, calculating first the signal velocities and then the required averages yields a non-vanishing velocity at cell face $k+\frac{1}{2}$. The effect is that the compression of cells k and $k+1$ does not stop as soon as the density plateau defined by the Rankine–Hugoniot–Taub relations is reached. The densities in these cells increase further on and the absolute values of the velocities increase again with reversed sign in order to conserve total momentum. This means that no shock waves are formed and the total system soon becomes unstable.

• *Step 7. Determination of the numerical fluxes.* At first we calculate the fluxes $F_{i\pm} = F(U_{i\pm}, q_{i\pm})$, where $F(U)$ is the physical flux of the conservation laws (23). The numerical fluxes are now determined by

$$G_{i+1/2}^{n+1/2} = \frac{\begin{pmatrix} b_{i+1/2}^{+} F_{i+}^{n+1/2} - b_{i+1/2}^{-} F_{(i+1)-}^{n+1/2} \\ + b_{i+1/2}^{+} b_{i+1/2}^{-} (U_{(i+1)-}^{n+1/2} - U_{i+}^{n+1/2}) \end{pmatrix}}{b_{i+1/2}^{+} - b_{i+1/2}^{-}}. \tag{8}$$

• *Step 8. Determination of the time-advanced quantities* U^{n+1}. The time-advanced values of the quantities U are obtained from those of the current cycle by adding the differences of incoming and outgoing numerical fluxes

$$U_i^{n+1} = U_i^n - \frac{\Delta t}{\Delta x}(G_{i+1/2}^{n+1/2} - G_{i-1/2}^{n+1/2}). \tag{9}$$

• *Step 9. Time-advanced values of rest-frame quantities.* In a last step, again, the system of Eqs. (4)–(7) has to be solved as outlined in Section 3 to provide a complete set of hydrodynamic variables at the beginning of the next computational cycle.

ACKNOWLEDGMENTS

The authors are grateful to Drs. J. P. Boris and D. L. Book for a prepublication version of the LCPFCT code, and one of the authors (J.A.M.) wishes to thank the Naval Research Laboratory for the hospitality and stimulating discussions there. This Research was sponsored by the Gesellschaft für Schwerionenforschung and by the Bundesministerium für Forschung und Technologie.

REFERENCES

1. A. Bamberger *et al.*, *Phys. Lett. B* **184**, 271 (1987).
2. R. Albrecht *et al.*, *Phys. Lett. B* **199**, 297 (1987).
3. G. Graebner, Ph. D. thesis, Frankfurt, 1985.
4. M. L. Norman and K. A. Winkler, in *Astrophysical Radiation Hydrodynamics* (Reidel, Dordrecht, 1986), p. 449.
5. J. P. Boris and D. L. Book, *J. Comput. Phys.* **11**, 38 (1973).
6. D. L. Book, J. P. Boris, and K. Hain, *J. Comput. Phys.* **18**, 248 (1975).
7. J. P. Boris and D. L. Book, *J. Comput. Phys.* **20**, 397 (1976).
8. J. P. Boris and D. L. Book, LCPFCT, preprint, 1989.
9. A. Harten, P. D. Lax, and B. van Leer, *SIAM Rev.* **25**, 35 (1983).
10. B. Einfeldt, *SIAM J. Numer. Anal.* **25**, 294 (1988).
11. B. Einfeldt, C.-D. Munz, P. L. Roe, and B. Sjögren, *J. Comput. Phys.*, to appear.
12. B. van Leer, *J. Comput. Phys.* **32**, 101 (1979).
13. P. Woodward and P. Colella, *J. Comput. Phys.* **54**, 115 (1984).
14. F. H. Harlow, A. A. Amsden, and J. R. Nix, *J. Comput. Phys.* **20**, 119 (1976).

15. G. Buchwald *et al.*, *Nucl. Phys. A* **428**, 297 (1984).
16. S. T. Zalesak, *J. Comput. Phys.* **31**, 335 (1979).
17. U. Katscher, diploma thesis, Frankfurt, 1990.
18. A. Harten, *J. Comput. Phys.* **49**, 357 (1983).
19. S. F. Davis, *SIAM J. Sci. Stat. Comput.* **9**, 445 (1988).
20. P. L. Roe, *J. Comput. Phys.* **43**, 357 (1981).
21. P. L. Roe, *Lecture Notes in Physics*, Vol. 141 (Springer-Verlag, New York, 1981), p. 354.
22. P. D. Lax, *Commun. Pure Appl. Math.* **7**, 159 (1954).
23. B. van Leer, *SIAM J. Sci. Stat. Comput.* **5**, 1 (1984).
24. C.-D. Munz, *J. Comput. Phys.* **77**, 18 (1988).
25. J. Centrella and J. R. Wilson, *Astrophys. J. Suppl.* **54**, 229 (1984).
26. A. H. Taub, *Phys. Rev.* **74**, 328 (1948).
27. J. Eisenberg and W. Greiner, *Nuclear Theory* (North-Holland, Amsterdam, 1987), p. 792.
28. D. H. Rischke, B. L. Friman, B. M. Waldhauser, H. Stöcker, and W. Greiner, *Phys. Rev. D* **41**, 111 (1990).
29. T. L. McAbee, J. R. Wilson, J. A. Zingman, and C. T. Alonso, *Mod. Phys. Lett. A* **4**, 983 (1989).
30. G. A. Sod, *J. Comput. Phys.* **27**, 1 (1978).